

Motility-induced temperature difference in coexisting phases

Suvendu Mandal,^{1,*} Benno Liebchen,^{1,2,†} and Hartmut Löwen^{1,‡}

¹*Institut für Theoretische Physik II: Weiche Materie,
Heinrich-Heine-Universität Düsseldorf, D-40225 Düsseldorf, Germany*
²*Theorie Weicher Materie, Fachbereich Physik, Technische Universität
Darmstadt, Hochschulstraße 12, 64289 Darmstadt, Germany*

(Dated: May 22, 2019)

Unlike in thermodynamic equilibrium where coexisting phases always have the same temperature, here we show that systems comprising “active” self-propelled particles can self-organize into two coexisting phases at different kinetic temperatures, which are separated from each other by a sharp and persistent temperature gradient. Contrasting previous studies which have focused on overdamped descriptions of active particles, we show that a “hot-cold-coexistence” occurs if and only if accounting for inertia, which is significant in a broad range of systems such as activated dusty plasmas, microflyers, whirling fruits or beetles at interfaces. Our results exemplify a route to use active particles to create a self-sustained temperature gradient across coexisting phases, a phenomenon, which is fundamentally beyond equilibrium physics.

Introduction.— In equilibrium systems, entropy maximization (or free energy minimization) requires thermal, mechanical and chemical equilibrium among coexisting phases. Conversely, in nonequilibrium no fundamental law forbids different temperatures in coexisting phases, evoking the question if a specific mechanism exists which can generate such a difference. Such a mechanism may appear counterintuitive, as heat-gradients, unless they are sustained by a localized heat-source such as a star performing nuclear fusion, usually cause processes opposing them and driving the system towards thermal equilibrium (unless for ideal isolation): For example, a temperature difference in the air evokes a balancing wind, and air friction cools down a radiator once switched off.

Here we report and systematically explore a surprisingly different scenario, where particles self-organize into coexisting phases sustaining different temperatures. This two temperature coexistence occurs spontaneously in a uniform system and remarkably, there is no heat flux at steady state, because the gradient in kinetic temperature is balanced by a self-sustained, opposite density gradient. A “hot” and a “cold” phase are allowed to coexist in principle, as the system we consider comprises self-propelled microparticles which allow the system to bypass equilibrium thermodynamics.

By now, we know that such microparticles, often described as “active Brownian particles” [1–5], can self-organize into a liquid phase, coexisting with a gas-phase, even when interacting purely repulsively [6–17]. Coined as “motility-induced phase separation”, or MIPS, this phenomenon has advanced to a key paradigm in the physics of self-propelled particles. When the microparticles are overdamped, like microorganisms in a solvent [18] or active colloidal microswimmers [19–23], they are equally fast in both phases. Hence, despite the presence of active microparticles, liquid and gas as emerging from MIPS have identical kinetic temperatures, just like for liquid-gas phase separation in equilibrium. (Note that

MIPS involves a slow-down of particles in regions of high density [2, 6]; which occurs however only for the ‘coarse grained self-propulsion’, not for the actual velocity determining the kinetic temperature, as further discussed below.)

When releasing the overdamped standard approximation, as relevant e.g. for beetles at interfaces [24], whirling fruits [25] microflyers [26] or activated dusty plasmas [27], both the phase diagram and the properties of the contained phases change dramatically, as we show in this Letter. In particular, while MIPS generally requires a sufficiently large self-propulsion speed v_0 to occur, specifically for underdamped particles it breaks down again if v_0 is too large, i.e. MIPS is reentrant in the presence of inertia [28]. This is because MIPS also requires particles to slow-down (regarding their directed motion) in regions of high density [2]: such a slow-down occurs instantaneously upon collisions of overdamped particles, but in the presence of inertia, particles bounce back from collisions and do not slow down much before experiencing subsequent collisions. Thus, at very large v_0 , underdamped particles can exchange their kinetic energies before slowing down much and MIPS breaks down.

To see which physical mechanism controls the kinetic temperature difference (to be distinguished from the effective temperature [29–32]) in coexisting phases, consider the collision of an active underdamped particle moving with a fixed orientation towards an elastically reflecting wall. This problem is equivalent to a bouncing ball experiencing friction and gravity (see Supplemental Material for details): while reaching a terminal speed (v_0) when falling in free space, the ball continuously slows down, when reflected by a wall, even when the collisions are elastic. Analogously, particles essentially move with v_0 in the gas phase, where they rarely collide, but slow down when entering the dense liquid phase, due to successive collisions with other particles (see Fig. 1). Notice that inelastic collisions among the particles provide an al-

| | |
|------------------------------|------------------------------------|
| persistence time | $\tau_p = 1/D_r$ |
| mean time between collisions | $\tau_c = \pi\sigma/(4v_0\varphi)$ |
| inertial time | $\tau_d = m/\gamma_t$ |

TABLE I. Relevant time scales in active underdamped particles.

ternative, but mechanistically unrelated, route to achieve a remarkable hot-cold coexistence, which has been discussed for vibrated granular particles, where particles dissipate energy due to inelastic collisions [33–35]. In contrast, for the microparticles we consider, no inelastic collisions are required: the emergence of coexisting temperatures is based on the interplay of activity and weak inertia.

Our results exemplify a generic route to use active particles to create a self-sustained temperature gradient across coexisting phases, a phenomenon, which is fundamentally beyond equilibrium physics. This contrasts the overdamped standard case, which has been predominantly explored in active matter physics so far and leads to a dynamics which can be essentially mapped onto an equilibrium system at a coarse grained level [2, 6] yielding a phase transition which is consistent with an equilibrium liquid-gas transition [36]. Thus, the existence of temperature differences in coexisting phases indicates a change of the nature of MIPS, when releasing the overdamped standard approximation: it changes from a liquid-gas like transition to a new type of phase transition having no counterpart in equilibrium. Accordingly, part of phenomenology of MIPS [6, 37–40], a key result in active matter physics, is even broader than anticipated previously - but was curtailed by the overdamped standard approximation in previous studies.

Model.— To demonstrate our results in detail, let us now consider a generic model for active underdamped particles in 2D, each having an internal drive, represented by an effective self-propulsion force $\mathbf{F}_{\text{SP},i} = \gamma_t v_0 \mathbf{u}(\theta_i)$ where $\mathbf{u}(\theta_i) = (\cos\theta_i, \sin\theta_i)$ is the direction of self-propulsion. The particles have identical diameters σ , masses m and moments of inertia I . They interact via an excluded-volume repulsive force \mathbf{F}_i (see Supplemental Material). Their velocities \mathbf{v}_i and orientations θ_i evolve as

$$\begin{aligned} m \frac{d\mathbf{v}_i}{dt} &= -\gamma_t \mathbf{v}_i + \mathbf{F}_i + \mathbf{F}_{\text{SP},i} + \sqrt{2k_B T_b \gamma_t} \boldsymbol{\eta}_i(t), \\ I \frac{d^2\theta_i}{dt^2} &= -\gamma_r \frac{d\theta_i}{dt} + \sqrt{2k_B T_b \gamma_r} \xi_i(t), \end{aligned} \quad (1)$$

where $\boldsymbol{\eta}_i$, ξ_i represent Gaussian white noise of zero-mean unit variance, T_b is the effective bath temperature and γ_t, γ_r are translational and rotational drag coefficients, yielding diffusion coefficients $D_{t,r} = k_B T_b / \gamma_{t,r}$.

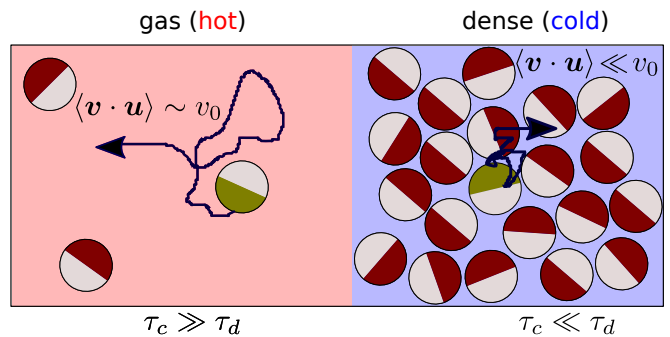


FIG. 1. Scheme of the phase-separated state associated with a hot-cold coexistence in underdamped active particles. Particles self-propel with the colored cap ahead (brown; greenish for the tagged particle). Active particles move with $\sim v_0$ in the gas phase, but can be an order of magnitude slower in the dense phase.

To understand the behavior of active underdamped particles, it is instructive to define three characteristic time scales (see table I): the persistence time $\tau_p = 1/D_r$, after which the directed motion of active particles is randomized by rotational diffusion, the mean time between collisions for a given particle $\tau_c = \pi\sigma/(4v_0\varphi)$, where $\varphi = N\pi\sigma^2/(4L_x L_y)$ is the area fraction, and the inertial time scale $\tau_d = m/\gamma_t$, characterizing the time a particle at rest needs to reach its terminal speed. (In principle, the moment of inertia I leads to an additional timescale (I/γ_r), but it turns out to be largely irrelevant to our results and is thus kept constant to $I = 0.33\epsilon\tau_p^2$ (see Supplementary Material).

Fixing the area fraction to a regime where MIPS can occur ($\varphi = 0.5$), the behavior of our system is mainly controlled by two parameters, which can be expressed as ratios of the relevant timescales: $M = \tau_d/\tau_p$, which is a reduced mass measuring the impact of inertia, and the Péclet number $\text{Pe} = v_0/(D_r\sigma) \propto \tau_p/(\tau_c\varphi)$ (see Supplemental Material), measuring the strength of self-propulsion by comparing ballistic to a diffusive motion.

Nonequilibrium phase diagram.— To explore the impact of inertia on the collective behavior of active particles, we first explore the phase-diagram using large-scale simulations based on LAMMPS [41]. If $M \rightarrow 0$, inertia plays no role and the particles are essentially overdamped. Accordingly, for $M \lesssim 10^{-4}$, we recover the usual behavior: at fixed area fraction $\varphi = 0.5$, the particles undergo MIPS [10, 12] when the Péclet number is large enough ($\text{Pe} \gtrsim 20$), leading to a dense liquid phase, coexisting with a gas phase (Fig. 2(a)), further characterized in Supplemental Material. For moderate inertia ($0.03 \leq M \leq 0.07$), we still require Pe to exceed a certain threshold to allow the system to phase separate into a liquid and a coexisting gas (Fig. 2(e)). However, when further increasing Pe , strikingly, MIPS disappears and the system remains in the disordered phase

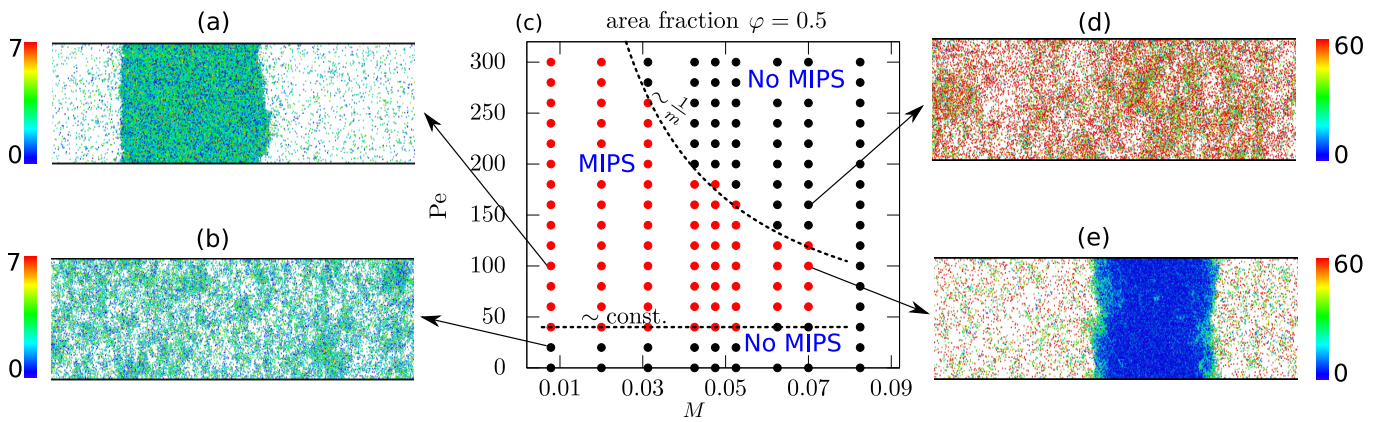


FIG. 2. Nonequilibrium phase diagram at $\varphi = 0.5$ (c). Panels (a), (b), (d), and (e) represent snapshots from our simulations ($L_x \times L_y = 350\sigma \times 70\sigma$) at state points indicated in the phase diagram. Each simulation has been performed in a box of size $L_x \times L_y = 850\sigma \times 170\sigma$, comprising $N \approx 10^5$ particles. Colors represent kinetic energies of individual particles in units of $k_B T$. A hot-cold coexistence is visible in panel (e). Dashed lines in (c) show scaling predictions for the phase boundary between the homogeneous and phase-separated state.

(Fig. 2(d)). Thus, MIPS is reentrant for underdamped active particles. Finally, when inertia is even stronger $M \gtrsim 0.08$, MIPS does not occur at all. Overall, this leads to the phase diagram shown in Fig. 2(c). The qualitative structure of this phase diagram can be understood based on simple scaling arguments. To see this, let us first remember how MIPS arises for overdamped particles: consider a particle self-propelling towards a small dense cluster of particles; when colliding, the particle stops and is blocked by the cluster, until rotational diffusion turns its self-propulsion direction away from the cluster on a timescale $\tau_p = 1/D_r$. When the time in between collisions τ_c is smaller than τ_p , the rate of particles entering the cluster exceeds the leaving-rate and the cluster rapidly grows [7, 9], later proceeding slowly towards phase separation. This criterion explains the existence of a (lower) critical Péclet number. Since both τ_c, τ_p are mass-independent, we expect the lower critical Pe number also to be mass-independent:

$$\tau_p \gtrsim \tau_c \quad \Rightarrow \quad \text{Pe}_1 = \text{const.} \quad (2)$$

as approximately observed in Fig. 2(c). To understand the upper critical Pe number, note that MIPS requires a localized slow-down of particles to occur. Thus, at very high collision rates (due to high Pe), underdamped particles bounce back multiple times on the inertial time scale τ_d , and can therefore not slow down locally. We, therefore, expect that MIPS occurs only if

$$\tau_c \gtrsim \tau_d \quad \Rightarrow \quad \text{Pe}_2 \propto 1/m, \quad (3)$$

which yields the scaling law $\text{Pe} \sim 1/m$ shown as the upper dashed line in Fig. 2(c) and corresponds to our simulation results.

Temperature difference in coexisting phases.— Let us now explore the properties of the resulting liquid and the

coexisting gas, in parameter regimes where MIPS takes place. While in the overdamped case ($M \rightarrow 0$), particles in the liquid and in the coexisting gas are equally fast on average as shown by the colors in Fig. 2(a), this changes dramatically when inertia becomes significant. Following the colors in Fig. 2(e) we see, strikingly, that particles in the liquid (blue dots) are much slower than in the gas (green, yellow and red dots). Before discussing the origin of this remarkable temperature difference, let us quantify it more detail. To this end, we define the kinetic temperature as $T_{\text{eff}}(x) = \frac{1}{2}m\langle v^2(x) \rangle$, which is the kinetic energy per particle, averaged along the lateral coordinate. As shown in Fig. 3(a), T_{eff} is uniform for $M = 10^{-5}$, but develops a massively nonuniform shape when increasing M to 0.05 (see Supplementary Movies S1 and S2, respectively). Fig. 3(c) quantifies the resulting temperature difference, showing $(T_{\text{gas}} - T_{\text{dense}})/T_{\text{dense}}$ as a function of M . Here, we see that the temperature in the dilute phase can be almost two orders of magnitude larger than in the dense phase. (Note that Fig. 3(c) shows that the temperature difference has a maximum at some M value before MIPS disappears, and then decreases again; this is probably a consequence of the fact, that the collision rate in the gas phase increases in the corresponding parameter domain, which cools the gas, as we will see below.) This is further reflected by the velocity distribution $P(v_x)$ in Fig. 3(b), showing a far-broader distribution for the gas phase than for the dense one, but only if inertia is significant (see inset).

Power-balance.— To understand the temperature difference quantitatively, we now derive a power-balance equation. Multiplying the translational part of Eq. (1) by \mathbf{v} , and averaging over all particles in a given phase, we obtain

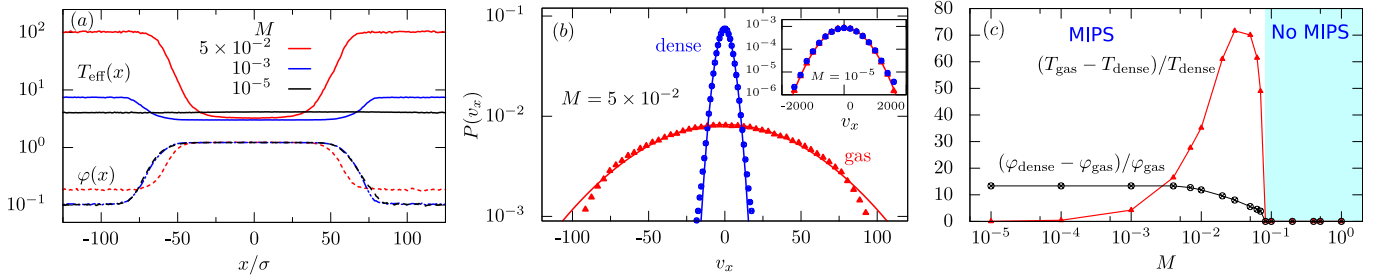


FIG. 3. (a) Spatial profiles of the effective temperature $T_{\text{eff}}(x) + 2.0$ (solid lines) and local area fraction $\varphi(x)$ (dashed lines) for different reduced masses M . (b) Steady-state distributions of particle velocities v_x for moderate inertia $M = 5 \times 10^{-2}$. Solid lines are fits to the Maxwell-Boltzmann distribution $P(v_x) = \sqrt{m/(2\pi T_{\text{eff}})} \exp[-mv_x^2/(2T_{\text{eff}})]$, where T_{eff} is the kinetic temperature. Inset: $P(v_x)$ for vanishing inertia $M = 10^{-5}$. (c) The relative temperature and area fraction difference between the two phases as a function of inertia. Other parameters: $\text{Pe} = 100$, $\varphi = 0.5$.

$$\frac{1}{2}m \frac{d\langle v^2(t) \rangle}{dt} = -\gamma_t \langle v^2(t) \rangle + \langle \mathbf{v}(t) \cdot \mathbf{F}(t) \rangle + \langle \mathbf{v}(t) \cdot \mathbf{F}_{\text{SP}}(t) \rangle + \sqrt{2k_B T_b \gamma_t} \langle \mathbf{v}(t) \cdot \boldsymbol{\eta}(t) \rangle. \quad (4)$$

Here, the left hand side equals the time derivative of the effective temperature $\partial T_{\text{eff}}/\partial t$; $\gamma_t \langle v^2(t) \rangle = 2T_{\text{eff}}/\tau_d$ describes the energy dissipation rate due to Stokes drag and $\langle \mathbf{v}(t) \cdot \mathbf{F}(t) \rangle$ represents the dissipated power due to interactions among the particles, which is negligible here since particle collisions are elastic, see Supplementary Fig. S4. The third-term $\langle \mathbf{v}(t) \cdot \mathbf{F}_{\text{SP}}(t) \rangle$ represents the self-propulsion power. The last-term is related to the bath temperature by the following relation $\sqrt{2k_B T_b \gamma_t} \langle \mathbf{v}(t) \cdot \boldsymbol{\eta}(t) \rangle = 2k_B T_b \gamma_t/m = 2k_B T_b/\tau_d$, which is identical in the gas and in the dense phase. Plugging these expressions into Eq. (4), and using that $\partial T_{\text{eff}}/\partial t = 0$ in each phase individually in steady state, we obtain

$$T_{\text{gas}} - T_{\text{dense}} = \frac{\tau_d}{2} [\langle \mathbf{v} \cdot \mathbf{F}_{\text{SP}} \rangle_{\text{gas}} - \langle \mathbf{v} \cdot \mathbf{F}_{\text{SP}} \rangle_{\text{dense}}]. \quad (5)$$

Therefore, if and only if $\tau_d \neq 0$, self-propulsion can create a temperature difference in coexisting phases. Since $\tau_d = 0$, in overdamped particles, both phases have the same kinetic temperature. In contrast, for underdamped particles we have $\tau_d \neq 0$. The contributions of the individual terms to the power balance is visualized in Supplementary Fig. S4, revealing that the self-propulsion power is much higher in the gas phase than in the dense phase and dominates the kinetic temperature (rather than diffusion as for overdamped particles). To see, why the self-propulsion power is different in the gas phase compared to the dense phase, we explore the distribution of the particle effective speeds $v_{\text{eff}} = \mathbf{v} \cdot \mathbf{u}$ in both phases; here $\langle \mathbf{v} \cdot \mathbf{F}_{\text{SP}} \rangle = \gamma_t v_0 \langle v_{\text{eff}} \rangle$. Thus, Figure 4 shows that the average effective speed in the gas phase is v_0 , whereas negative speed values are rare, showing that particles in the gas phase rarely move against their self-propulsion direction (Fig. 1, left panel). This suggests

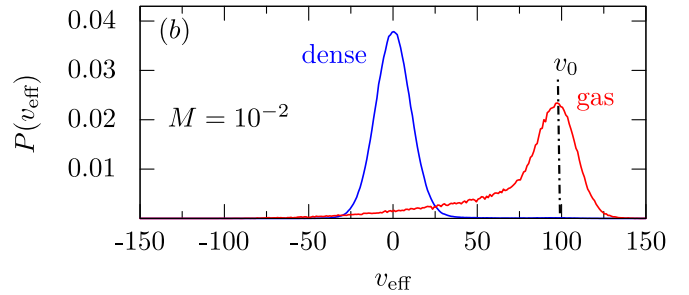


FIG. 4. Probability distributions of effective speeds in the gas phase as well as in the dense phase. Other parameters: $\text{Pe} = 100$, $\varphi = 0.5$.

that $\langle \mathbf{v} \cdot \mathbf{F}_{\text{SP}} \rangle_{\text{gas}} \sim \gamma_t v_0^2$. In contrast, in the dense phase, the effective particle speed is almost symmetrically distributed around 0, which results from the fact that particles have no space to move and bounce back after each collision; thus, they move against their self-propulsion direction about half of the time (Fig. 1, right panel), which implies $\langle \mathbf{v} \cdot \mathbf{F}_{\text{SP}} \rangle_{\text{dense}} \sim 0$.

Conclusion.— Unlike equilibrium systems, self-driven active particles can self-organize into a liquid and a coexisting gas phase at different temperatures. This result exemplifies a route to use self-driven particles to create a self-sustained temperature gradient, which might serve, in principle, as a novel paradigm to create isolating layers at the microscale, e.g. to keep bodies at different temperatures.

On a more fundamental level, our results show that motility-induced phase separation, one of the best explored phenomenon in active matter research, is fundamentally different from a liquid-gas phase separation – an insight which has been curtailed by the focus on overdamped particles so far. As a consequence, the phenomenology of motility-induced phase separation is even richer than anticipated previously – it can, in particular, lead to phenomena at the macroscale which are fundamentally beyond equilibrium physics.

For future studies, it would also be interesting to study the effect of inertia on anisotropic active particles [42–45] where translational and rotational motions are coupled. Specifically for such particles, ref. [46] has recently observed (but hardly analyzed) the occurrence of different kinetic energies in coexisting phases, suggesting that the present findings survive for particles of nonspherical shape.

An interesting challenge would also be to derive a microscopic theory for motility-induced phase separation in underdamped particles to predict the joint temperature and density profiles across the interface between the two coexisting states [47]. Such an approach needs to be designed for non-isothermal situations as considered recently in Enskog kinetic theories [48, 49] or in dynamical density functional theory [50, 51].

We thank Christian Scholz and Alexei Ivlev for fruitful discussions. This work is supported by the German Research Foundation (Grant No. LO 418/23-1)

* mandal@hhu.de

† liebchen@fkp.tu-darmstadt.de

‡ hlowen@hhu.de

- [1] P. Romanczuk, M. Bär, W. Ebeling, B. Lindner, and L. Schimansky-Geier, “Active brownian particles,” *Eur. Phys. J. Spec. Top.* **202**, 1 (2012).
- [2] M. E. Cates and J. Tailleur, “Motility-induced phase separation,” *Annu. Rev. Condens. Matter Phys.* **6**, 219 (2015).
- [3] R. Ni, M. A. C. Stuart, and M. Dijkstra, “Pushing the glass transition towards random close packing using self-propelled hard spheres,” *Nat. Commun.* **4**, 2704 (2013).
- [4] C. Kurzthaler, C. Devailly, J. Arlt, T. Franosch, W. C. K. Poon, V. A. Martinez, and A. T. Brown, “Probing the spatiotemporal dynamics of catalytic janus particles with single-particle tracking and differential dynamic microscopy,” *Phys. Rev. Lett.* **121**, 078001 (2018).
- [5] R. G. Winkler, A. Wysocki, and G. Gompper, “Virial pressure in systems of spherical active brownian particles,” *Soft Matter* **11**, 6680–6691 (2015).
- [6] J. Tailleur and M. E. Cates, “Statistical mechanics of interacting run-and-tumble bacteria,” *Phys. Rev. Lett.* **100**, 218103 (2008).
- [7] Y. Fily and M. C. Marchetti, “Athermal phase separation of self-propelled particles with no alignment,” *Phys. Rev. Lett.* **108**, 235702 (2012).
- [8] A. Patch, D. M. Sussman, D. Yllanes, and M. C. Marchetti, “Curvature-dependent tension and tangential flows at the interface of motility-induced phases,” *Soft Matter* **14**, 7435–7445 (2018).
- [9] I. Buttinoni, J. Bialké, F. Kümmel, H. Löwen, C. Bechinger, and T. Speck, “Dynamical clustering and phase separation in suspensions of self-propelled colloidal particles,” *Phys. Rev. Lett.* **110**, 238301 (2013).
- [10] J. Stenhammar, A. Tiribocchi, R. J. Allen, D. Marenduzzo, and M. E. Cates, “Continuum theory of phase separation kinetics for active brownian particles,” *Phys. Rev. Lett.* **111**, 145702 (2013).
- [11] J. Stenhammar, D. Marenduzzo, R. J. Allen, and M. E. Cates, “Phase behaviour of active brownian particles: the role of dimensionality,” *Soft Matter* **10**, 1489–1499 (2014).
- [12] G. S. Redner, M. F. Hagan, and A. Baskaran, “Structure and dynamics of a phase-separating active colloidal fluid,” *Phys. Rev. Lett.* **110**, 055701 (2013).
- [13] P. Digregorio, D. Levis, A. Suma, L. F. Cugliandolo, G. Gonnella, and I. Pagonabarraga, “Full phase diagram of active brownian disks: From melting to motility-induced phase separation,” *Phys. Rev. Lett.* **121**, 098003 (2018).
- [14] Z. Mokhtari, T. Aspelmeier, and A. Zippelius, “Collective rotations of active particles interacting with obstacles,” *Europhys. Lett.* **120**, 14001 (2017).
- [15] A. P. Solon, J. Stenhammar, M. E. Cates, Y. Kafri, and J. Tailleur, “Generalized thermodynamics of motility-induced phase separation: phase equilibria, laplace pressure, and change of ensembles,” *New J. Phys.* **20**, 075001 (2018).
- [16] D. Levis, J. Codina, and I. Pagonabarraga, “Active brownian equation of state: metastability and phase coexistence,” *Soft Matter* **13**, 8113–8119 (2017).
- [17] J. T. Siebert, F. Dittrich, F. Schmid, K. Binder, T. Speck, and P. Virnau, “Critical behavior of active brownian particles,” *Phys. Rev. E* **98**, 030601(R) (2018).
- [18] J. Elgeti, R. G. Winkler, and G. Gompper, “Physics of microswimmers—single particle motion and collective behavior: a review,” *Rep. Prog. Phys.* **78**, 056601 (2015).
- [19] C. Bechinger, R. Di Leonardo, H. Löwen, C. Reichhardt, G. Volpe, and G. Volpe, “Active particles in complex and crowded environments,” *Rev. Mod. Phys.* **88**, 045006 (2016).
- [20] H.-W. Huang, F. E. Uslu, P. Katsamba, E. Lauga, M. Sakar, and B. Nelson, “Adaptive locomotion of artificial microswimmers,” *Sci. Adv.* **5**, eaau1532 (2019).
- [21] A. Aubret, S. Ramanarivo, and J. Palacci, “Eppur si muove, and yet it moves: Patchy (phoretic) swimmers,” *Curr. Opin. Colloid Interface Sci.* **30**, 81–89 (2017).
- [22] A. Aubret and J. Palacci, “Diffusiophoretic design of self-spinning microgears from colloidal microswimmers,” *Soft Matter* **14**, 9577–9588 (2018).
- [23] C. Maggi, M. Paoluzzi, L. Angelani, and R. Di Leonardo, “Memory-less response and violation of the fluctuation-dissipation theorem in colloids suspended in an active bath,” *Scientific reports* **7**, 17588 (2017).
- [24] H. Mukundarajan, T. C. Bardon, D. H. Kim, and M. Prakash, “Surface tension dominates insect flight on fluid interfaces,” *J. Exp. Biol.* **219**, 752–766 (2016).
- [25] J. Rabault, R. A. Fauli, and A. Carlson, “Curving to fly: Synthetic adaptation unveils optimal flight performance of whirling fruits,” *Phys. Rev. Lett.* **122**, 024501 (2019).
- [26] C. Scholz, S. Jahanshahi, A. Ldov, and H. Löwen, “Inertial delay of self-propelled particles,” *Nat. Commun.* **9**, 5156 (2018).
- [27] G. E. Morfill and A. V. Ivlev, “Complex plasmas: An interdisciplinary research field,” *Rev. Mod. Phys.* **81**, 1353–1404 (2009).
- [28] A. Suma, G. Gonnella, D. Marenduzzo, and E. Orlandini, “Motility-induced phase separation in an active dumbbell fluid,” *EPL* **108**, 56004 (2014).
- [29] L. F. Cugliandolo, “The effective temperature,” *J. Phys. A* **44**, 483001 (2011).
- [30] C. Nardini, E. Fodor, E. Tjhung, F. van Wijland,

- J. Tailleur, and M. E. Cates, “Entropy production in field theories without time-reversal symmetry: Quantifying the non-equilibrium character of active matter,” *Phys. Rev. X* **7**, 021007 (2017).
- [31] D. Levis and L. Berthier, “From single-particle to collective effective temperatures in an active fluid of self-propelled particles,” *EPL* **111**, 60006 (2015).
- [32] Z. Preisler and M. Dijkstra, “Configurational entropy and effective temperature in systems of active brownian particles,” *Soft Matter* **12**, 6043–6048 (2016).
- [33] Y. Komatsu and H. Tanaka, “Roles of energy dissipation in a liquid-solid transition of out-of-equilibrium systems,” *Phys. Rev. X* **5**, 031025 (2015).
- [34] K. Roeller, J. P. D. Clewett, R. M. Bowley, S. Herminghaus, and M. R. Swift, “Liquid-gas phase separation in confined vibrated dry granular matter,” *Phys. Rev. Lett.* **107**, 048002 (2011).
- [35] T. Schindler and S. C. Kapfer, “Nonequilibrium steady states, coexistence, and criticality in driven quasi-two-dimensional granular matter,” *Phys. Rev. E* **99**, 022902 (2019).
- [36] D. Levis, J. Codina, and I. Pagonabarraga, “Active brownian equation of state: metastability and phase coexistence,” *Soft Matter* **13**, 8113 (2017).
- [37] P. Krinninger, M. Schmidt, and J. M. Brader, “Nonequilibrium phase behavior from minimization of free power dissipation,” *Phys. Rev. Lett.* **117**, 208003 (2016).
- [38] A. P. Solon, J. Stenhammar, M. E. Cates, Y. Kafri, and J. Tailleur, “Generalized thermodynamics of phase equilibria in scalar active matter,” *Phys. Rev. E* **97**, 020602 (2018).
- [39] T. Speck, J. Bialké, A. M. Menzel, and H. Löwen, “Effective cahn-hilliard equation for the phase separation of active brownian particles,” *Phys. Rev. Lett.* **112**, 218304 (2014).
- [40] A. Wysocki, R. G. Winkler, and G. Gompper, “Cooperative motion of active brownian spheres in three-dimensional dense suspensions,” *EPL* **105**, 48004 (2014).
- [41] S. Plimpton, “Fast parallel algorithms for short-range molecular dynamics,” *J. Comput. Phys.* **117**, 1–19 (1995).
- [42] N. H. P. Nguyen, D. Klotsa, M. Engel, and S. C. Glotzer, “Emergent collective phenomena in a mixture of hard shapes through active rotation,” *Phys. Rev. Lett.* **112**, 075701 (2014).
- [43] S. Farhadi, S. Machaca, J. Aird, B. O. T. Maldonado, S. Davis, P. E. Arratia, and D. J. Durian, “Dynamics and thermodynamics of air-driven active spinners,” *Soft Matter* **14**, 5588–5594 (2018).
- [44] G. Kokot, S. Das, R. G. Winkler, G. Gompper, I. S. Aranson, and A. Snezhko, “Active turbulence in a gas of self-assembled spinners,” *Proc. Natl. Acad. Sci.* **114**, 12870–12875 (2017).
- [45] A. Aubret, M. Youssef, S. Sacanna, and J. Palacci, “Targeted assembly and synchronization of self-spinning microgears,” *Nat. Phys.* **14**, 1114 (2018).
- [46] I. Petrelli, P. Digregorio, L. F. Cugliandolo, G. Gonnella, and A. Suma, “Active dumbbells: Dynamics and morphology in the coexisting region,” *Eur. Phys. J. E* **41**, 128 (2018).
- [47] K. Miyazaki, Y. Nakayama, and H. Matsuyama, “Entropy anomaly and linear irreversible thermodynamics,” *Phys. Rev. E* **98**, 022101 (2018).
- [48] J. J. Brey, V. Buzón, P. Maynar, and M. I. García de Soria, “Hydrodynamics for a model of a confined quasi-two-dimensional granular gas,” *Phys. Rev. E* **91**, 052201 (2015).
- [49] V. Garzó, R. Brito, and R. Soto, “Enskog kinetic theory for a model of a confined quasi-two-dimensional granular fluid,” *Phys. Rev. E* **98**, 052904 (2018).
- [50] R. Wittkowski, H. Löwen, and H. R. Brand, “Extended dynamical density functional theory for colloidal mixtures with temperature gradients,” *J. Chem. Phys.* **137**, 224904 (2012).
- [51] J. G. Anero, P. Español, and P. Tarazona, “Functional thermo-dynamics: A generalization of dynamic density functional theory to non-isothermal situations,” *J. Chem. Phys.* **139**, 034106 (2013).
- [52] J. D. Weeks, D. Chandler, and H. C. Andersen, “Role of repulsive forces in determining the equilibrium structure of simple liquids,” *J. Chem. Phys.* **54**, 5237–5247 (1971).
- [53] Q.-L. Lei, M. P. Ciamarra, and R. Ni, “Nonequilibrium strongly hyperuniform fluids of circle active particles with large local density fluctuations,” *Sci. Adv.* **5**, eaau7423 (2019).
- [54] C. Rycroft, “Voro++: A three-dimensional voronoi cell library in c++,” *Chaos* **19**, 041111 (2009).

SUPPLEMENTARY MATERIAL

SIMULATIONS

Simulations are performed with a slightly modified version of LAMMPS [41], which integrates the equations of motion given in Eq. (1) using the Euler method. The conservative force on particle i from particle j is $\mathbf{F}_i = -\nabla_i u(r_{ij})$, which results from a purely repulsive WCA potential [52]:

$$u(r_{ij}) = \begin{cases} 4\epsilon\left[\left(\frac{\sigma}{r_{ij}}\right)^{12} - \left(\frac{\sigma}{r_{ij}}\right)^6\right] + \epsilon, & r_{ij}/\sigma \leq 2^{1/6} \\ 0, & r_{ij}/\sigma > 2^{1/6} \end{cases}$$

where $\epsilon = k_B T$ is the interaction strength, and r_{ij} is the distance between particles i and j . The equations of motion are integrated with a time step $\delta t = 10^{-5}\tau_p$. Recent experiments [26] on microflyers reveal that diffusion coefficients (D_r and D_t) and friction coefficients (γ_r and γ_t) are not related by the Stokes-Einstein relation. Thus, for simplicity, we choose $\gamma_t = \gamma_r/\sigma^2$ as shown, e.g., in Ref. [53].

In order to clarify the importance of the moment of inertia I , we have performed simulations with two different moments of inertia $I = 0.33\epsilon\tau_p^2$ (Fig. 2(c) in the main text) and $I = 0.066\epsilon\tau_p^2$ (Supplementary Fig. 5). These two figures display qualitatively similar results, which implies that we are close to overdamped rotational dynamics, where $I = 0$.

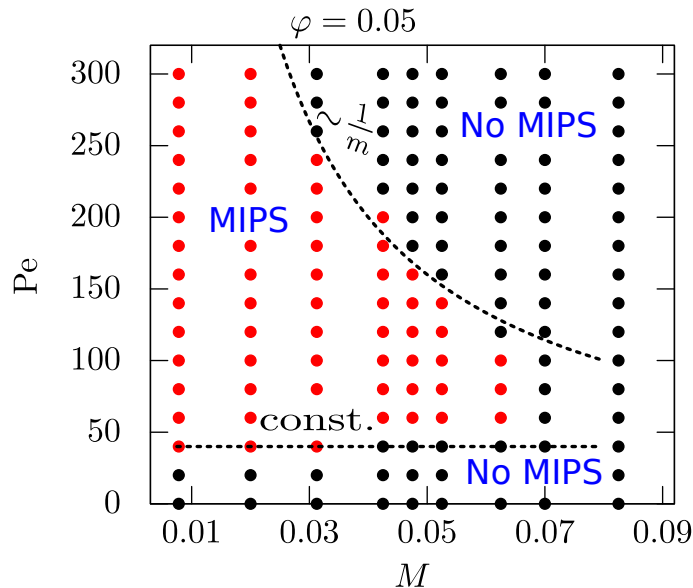


FIG. 5. Nonequilibrium phase diagram same as Fig. 2(c), but now for $I = 0.066\epsilon\tau_p^2$.

BOUNCING BALL PICTURE

To develop an intuition for the emergence of temperature differences let us exploit a simple formal analogy: the dynamics of an active particle with fixed orientation, which is elastically reflected by a fixed obstacle, is identical to the dynamics of an elastically bouncing ball under the influence of gravity (representing self-propulsion) and Stokes drag (Fig. 6(a)). To characterize the bouncing dynamics, we show the vertical position $y(t)$ as a function of time t in Fig. 6. For vanishing drag, $\gamma_t = 0$, energy is conserved and the ball bounces periodically without slowing down (Fig. 6(b)). However, when experiencing drag, the ball, initially at rest, accelerates due to gravity to a velocity which cannot exceed v_0 before hitting the fixed obstacle (Fig. 6(c) and inset). The ball bounces back elastically, preserving its speed upon the collision, but now ascends against the gravitational force to a turning point below the starting position. From here, the ball accelerates towards the obstacle again, but has less space to accelerate this time. Thus, each time the ball hits the obstacle, it is slower. The same slow-down mechanism applies to a particle entering the dense phase and encountering a series of collisions, each time bouncing back, against its self-propulsion direction, and

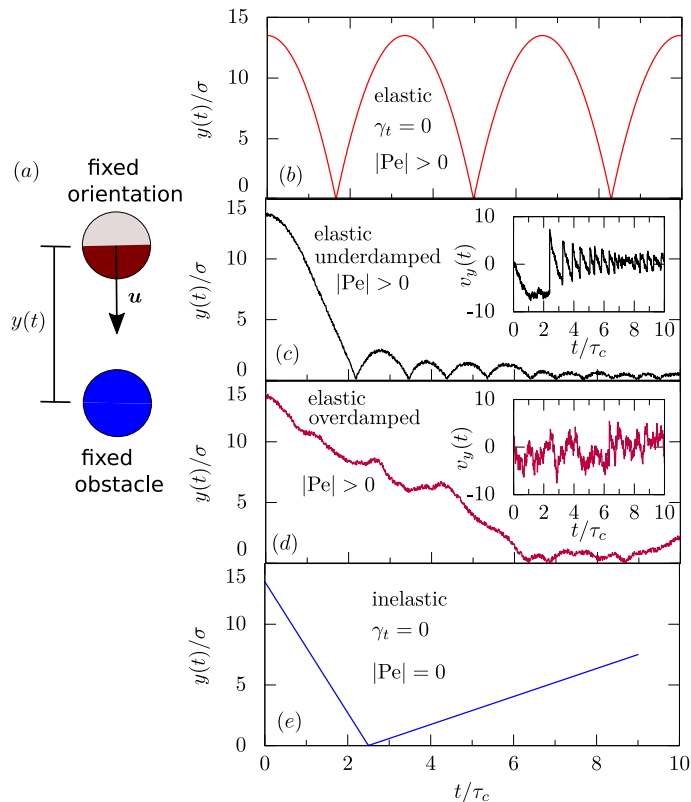


FIG. 6. (a) A ball with fixed orientation bounces back elastically from a fixed obstacle (blue particle). Typical trajectories (and velocities in insets) of a bouncing ball for (b) vanishing drag $\gamma_t = 0$, (c) finite drag $\gamma_t \neq 0$ (underdamped), and (d) infinite drag $\gamma_t = \infty$ (overdamped). (e) A typical trajectory of a ball when it encounters an inelastic collision rather than drag.

having less space to accelerate. This is in stark contrast to the behavior in the gas phase, where collisions are rare and particles have enough time to reach their terminal speed v_0 in between collisions. Thus, the active gas is much ‘hotter’ than the active liquid. The behavior of an overdamped bouncing ball is yet different (Fig. 6(d) and inset): this ball reaches its terminal speed instantaneously; when hitting the obstacle, it does not bounce back, and does not move any further, apart from translational diffusion. Here, while directed motion immediately stops when hitting the obstacle, the actual velocity of the particle hardly changes: This is because the instantaneous speed of overdamped particles is dominated by the diffusive micromotion, not by self-propulsion. Consequently, overdamped particles are equally fast in the gas and in the liquid, yielding identical temperatures in both phases – as in equilibrium. Finally, to contrast the present slow-down mechanism, crucially based on self-propulsion, from the scenario in vibrated granular particles, let us emphasize that the latter corresponds to a ball experiencing inelastic collisions, i.e. to a case where kinetic energy is drained from the system upon a collision.

NONEQUILIBRIUM PHASE DIAGRAM

To construct the phase diagram, an elongated box with periodic boundary conditions is used. Simulations were run up to $10^5 \tau_p$ in order to reach the steady state. To characterize the phase-separation, we measure the distribution $P(\varphi_{\text{loc}})$ of the local free-area φ_{loc} of active underdamped particles using the Voronoi tessellation method [54] (see Supplementary Fig. 7). Once the free-area distribution is bimodal, we identify it as a phase-separated state.

AREA FRACTION DIFFERENCE IN COEXISTING PHASES

In the phase-separated state, we can measure the local area fractions in the two different phases by dividing the simulation box into slabs of width $\simeq 0.5\sigma$. We find that the area fraction profiles (dashed lines) in Fig. 3(a) in the

main text are similar to ABPs and can be fitted to a hyperbolic tangent function

$$\varphi(x) = \frac{1}{2}(\varphi_{\text{dense}} + \varphi_{\text{gas}}) - \frac{1}{2}(\varphi_{\text{dense}} - \varphi_{\text{gas}}) \tanh \left[\frac{2(x - x_0)}{w} \right], \quad (6)$$

where x_0 and w are the location and width of the gas-liquid interface. We extract the corresponding area fractions of the gas phase φ_{gas} and the dense phase φ_{dense} by fitting each side of the interface using Eq. (6). In Fig. 3(c) (in the main text), we plot the relative area fraction difference $(\varphi_{\text{dense}} - \varphi_{\text{gas}})/\varphi_{\text{gas}}$ in coexisting phases by varying inertia while keeping the Péclet number fixed at $\text{Pe} = 100$. Notably we find that the area fraction difference between the two phases is 10 times higher than the gas phase and interfacial width $w \simeq 20\sigma$. As we move from phase-separated to a homogeneous state with increasing inertia M at fixed Pe , the relative area fraction decreases monotonically towards a critical inertia $M \approx 0.08$. This behavior is similar to the first-order-phase transition, but occurs in a non-equilibrium setup. Most importantly, the control parameter is inertia M instead of the thermodynamic temperature.

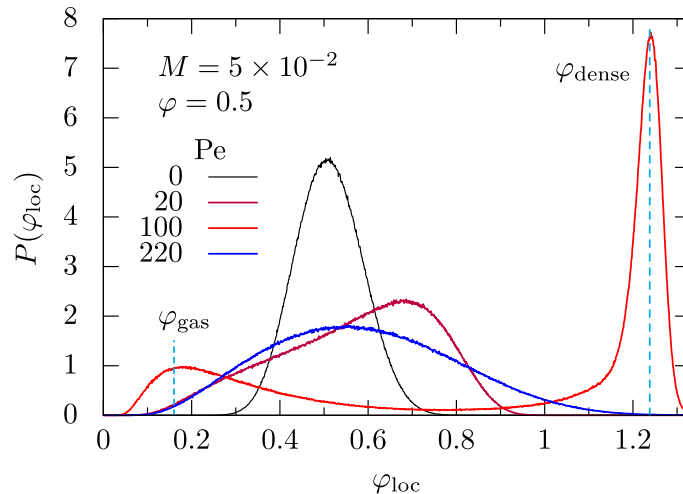


FIG. 7. Local free-area distributions for various Péclet numbers at fixed inertia $M = 5 \times 10^{-2}$ and global area fraction $\varphi = 0.5$. The distribution is peaked around the overall area fraction in equilibrium ($\text{Pe} = 0$). It broadens near the critical Péclet number $\text{Pe} = 20$. For $\text{Pe} = 100$, the distribution becomes bimodal as the system phase separates into a gas and a dense phase. As Pe is increased further, it becomes unimodal (homogeneous) again.

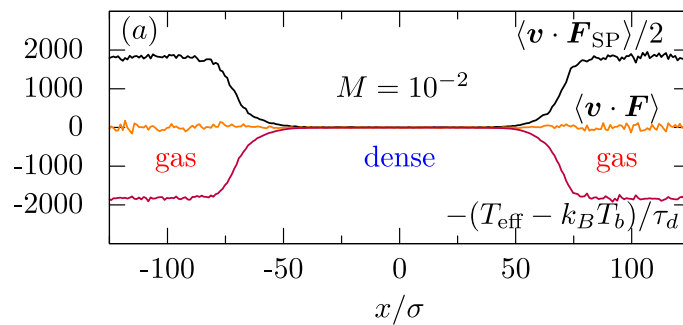


FIG. 8. Power balance in the phase-separated state, where the injected power by active forces is balanced by energy dissipation rate due to Stokes drag.

LEGENDS TO MOVIES

In all movies $\varphi = 0.5$, $L_x \times L_y = 850\sigma \times 170\sigma$, $N = 10^5$, $\text{Pe} = 100$, while reduced mass M and reduced temperature $T^* = T_{\text{eff}}/k_B T$ are provided for each movie. The simulation time t is measured in units of τ_p .

1. **Movie S1:** Underdamped active particles with $M = 10^{-5}$. Here, coexisting phases have the same temperature as shown by the colors, just like in equilibrium physics.

2. **Movie S2:** Underdamped active particles with $M = 0.05$. A massive temperature difference emerges between the two phases. In particular, particles in the dense phase (blue dots) are 'colder' than in the gas phase (green, yellow and red dots).